A Reactivity-controlled Epitaxial Growth Strategy for Large-sized Nanocrystal Synthesis

Zhiwei Long
Mingrui Liu
Beijing Institute of Technology
Xian-gang Wu
Beijing Institute of Technology
Kai Gu
Beijing Institute of Technology
Gaoling Yang
Beijing Institute of Technology
Zhuo Chen
BOE Technology Group Co., Ltd.
Yang Liu
BOE Technology Group Co., Ltd.
Ronghui Liu
General Research Institute for Nonferrous Metals
Haizheng Zhong (hzzhong@bit.edu.cn)
Beijing Institute of Technology https://orcid.org/0000-0002-2662-7472

Article

Keywords:

Posted Date: March 28th, 2022

DOI: https://doi.org/10.21203/rs.3.rs-1424634/v1

Version of Record: A version of this preprint was published at Nature Synthesis on January 12th, 2023.
See the published version at https://doi.org/10.1038/s44160-022-00210-5.

Abstract

Large-sized ZnSe nanocrystals are expected to emit pure-blue-light between 455-475 nm for display applications, however, haven't been achieved up to date. By analyzing the influence of the reactivity of Zn and Se precursors, we found that the final size of ZnSe nanocrystals via hot-injection has a critical value that can be varied by ligands or precursors. To describe the key factors in determining the final size of ZnSe nanocrystals, we propose a nuclei number-considered LaMer model based on the Maxwell-Boltzmann distribution of crystal embryos. As a result, a general strategy of reactivity-controlled epitaxial growth (RCEG) was developed to synthesize large-sized ZnSe nanocrystals through sequential injection of high-reactivity and low-reactivity Zn (Se) precursors. The resulted large-sized ZnSe nanocrystals show pure-blue emission between 455-470 nm. We further fabricated efficient and stable large-sized ZnSe/ZnS core-shell nanocrystals with photoluminescence quantum yields up to 60%. Moreover, the RCEG strategy is versatile to synthesize large-sized CdSe and PbSe nanocrystals with average size over 35 nm. The hybridization of quantum confined effects and classical surface effects in these large-sized semiconductor nanocrystals, which will open up new directions for fundamental research and application explorations.

Introduction

Semiconductor nanocrystals (NCs), also known as quantum dots (QDs), have been intensively investigated due to their well-known size dependent effects and solution processability, resulting in a big family of functional nanomaterials with tunable optical properties for many cutting-edge technologies, including display, lighting, photodetection, solar cells, etc[1,2]. In the field of display technology, CdSe and InP based nanocrystals have attracted significant attentions from scientific and industrial communities[3–6]. In particularly, they are considered as suitable printing inks for fabricating electroluminescence display panels[7–8]. Blue emitter with peaks of 455–475 nm is an urgent need to open up the industrialization of nanocrystals-based printing display technology[9]. ZnSe nanocrystals has been considered as potential blue emitters in view of its suitable band-gap (2.7 eV)[10–13]. Owing to the quantum confinement effect, the fabrication of large-sized ZnSe nanocrystals is of vital importance to tune their emission into pure blue region.

After more than 30 years' efforts, a thorough investigation of nanocrystals synthesis resulted in the state-of-the-art CdSe nanocrystals as well as the corresponding nucleation and growth mechanisms[14–21]. Nevertheless, there are few reports on CdSe nanocrystals with average size over 10 nm[22]. Even applying a multiple precursor injection method, the average size of giant CdSe based core-shell nanocrystals was still limited to 20 nm[23–25]. With the increase of nanocrystal's size, surface chemical potential decreases due to the reduction of surface to volume ratio[19]. Under high concentration or multiple injection conditions, monomers tend to grow epitaxially on crystal planes with higher chemical potential[26,27], resulting in the formation of anisotropic nanocrystals such as nanorods[28], nanosheets[29], or branched-

nanocrystals[30]. Similar anisotropic structures have been also observed in ZnSe-based nanocrystals[31–33]. Hence, it has been a great challenge to fabricate large-sized nanocrystals with isotropic shapes.

In this work, we investigated the influence of reactivity of Zn and Se precursors on the nucleation and growth of ZnSe nanocrystals via hot-injection method. Based on the experimental results and previous theoretical models, we developed a nuclei number-considered Lamer model to illustrate the correlation between the final size of nanocrystals and the nuclei number. A general strategy of reactivity-controlled epitaxial growth (RCEG) was proposed to synthesize large-sized ZnSe nanocrystals with average size over 35 nm. The resulted large-sized ZnSe nanocrystals show pure blue emission between 455–470 nm with narrow PL width (16–25 nm FWHM). After coating ZnS shell, we obtained nearly spherical ZnSe/ZnS core-shell nanocrystals with PLQY of 60%, which are promising candidates for display application. The RCEG strategy was successfully extended to synthesize large-sized CdSe and PbSe nanocrystals with average size over 70 nm. Except for the display application, the available large-sized nanocrystals combining the quantum confined effects and classical surface effects, will provide new opportunities for functionality-oriented studies such as photocatalysis, solar cells, and other optoelectronic devices.

Reactivity-control of ZnSe nanocrystals synthesis.

Considering the ZnSe nanocrystals synthesis, most of the previous studies adapted the reaction routes from CdSe nanocrystals, using zinc carboxylates (zinc oleate, zinc stearate) and selenium coordinates (Se-TOP, Se-ODE) as precursors[9–13, 31–35]. Because the high formation energy of ZnSe[36], high reactivity precursors are much preferred for the synthesis of ZnSe nanocrystals. To our knowledges, there are few works considering how the reactivity of precursors affect the nucleation and growth of ZnSe nanocrystals. In general, the cationic precursors are metal-organic coordinated compounds. The reactivity is mainly determined by the bonds between cationic and coordinated functional group[37]. In this work, we design a simple route to regulate the reactivity of Zn precursors. A high reactive Zn precursor of $[Zn(OAc)_2]$-OLA complex was prepared by dissolving $Zn(OAc)_2$ into mixed solvents of oleylamine (OLA) and 1-octadecene (ODE), of which the reactivity can be modulated by adding oleic acid (OA) as co-ligands due to the strong binding between zinc and carboxyl (schematic diagram as shown in figure S1). The decomposition of OA-$[Zn(OAc)_2]$-OLA complexes into ZnO nanoparticles can be applied to determine their reactivity by monitoring the UV-vis absorption spectra at different temperature intervals (detailed in figure S2). As shown in figure S6a, the decomposition temperature of OA-$[Zn(OAc)_2]$-OLA complexes increased with the OA/OLA ratio increasing, implying the reactivity decreasing.

By regulating the reactivity of OA-$[Zn(OAc)_2]$-OLA complex and Se-X coordinates (X = DPP, TOP, ODE), we then investigated the influence of precursors reactivity on the nucleation and growth of ZnSe nanocrystals. Nucleation temperature indicates the temperature at which the formation of ZnSe nanocrystals is initiated. The precursor reactivity can be characterized by comparing the nucleation temperature of the reaction between Zn and Se precursors. In our work, the nucleation temperature was recorded by monitoring the appearance of a distinct exciton absorption peak in the UV-vis absorption

spectra (detailed in figure S3-S5). As shown in figure S6b, the nucleation temperature can be tuned over a wide range (140–280°C) by implementing different reactivity Zn and Se precursors. It is noticed that the nucleation temperature of the reaction between OA-[$Zn(OAc)_2$]-OLA and Se-X coordinates increased with the concentration of OA increasing, confirming that the reactivity of OA-[$Zn(OAc)_2$]-OLA reduce with the increase of OA concentration. Moreover, the nucleation temperature can also be varied using different Se-X precursors with a reactivity order of Se-DPP > Se-TOP > Se-ODE (see figure S6b).

We further studied the effects of the reactivity of precursors on the nucleation and growth of ZnSe nanocrystals via hot-injection approach. Figure 1a-1d show the evolution of absorption and PL spectra of ZnSe nanocrystals with reaction time under different Zn and Se precursors with various reactivity. The injection of Se-X precursor into Zn precursor solution at high temperature prompts the formation of ZnSe monomers as well as the subsequent formation of ZnSe nuclei. With the reaction prolonging, the ZnSe nuclei undergo a diffusion-controlled growth. When the ZnSe monomers are completely consumed, the growth of ZnSe nanocrystals stopped, which is evidenced by slight change of UV and PL spectra. As shown in Fig. 1e, the use of lower reactivity precursors can result in a narrower FWHM and shorter PL Peak wavelength. To track the size evolution with reaction time prolonging, an equation that correlating ZnSe spectra with particle size is feasible[38]. Here, we plotted the correlations between the average sizes of resulted ZnSe nanocrystals with their PL emission peaks (Fig. 1f, the fitting formula shown in the method section). For most of the synthesis, the resulted ZnSe nuclei underwent an exponential growth process at the beginning, and then approach to a critical diameter with the reaction prolonging. As summarized in Fig. 1g, the maximum size of resulted ZnSe nanocrystals was limited to ~ 5 nm with a corresponding PL peak at around 425 nm when using Se-DPP and OA-[$Zn(OAc)_2$]-OLA (OA: OLA = 0.2) as precursors.

Insights into nucleation and growth of monodisperse nanocrystals.

To understand the key factors in determining the final size of ZnSe nanocrystals, we adapted the modified Lamer models that developed from classical CdSe nanocrystals synthesis[39–42]. As shown in Fig. 2a, a typical colloidal semiconductor nanocrystal synthesis includes three stages. In the first stage, the metal (A) and nonmetal (B) precursors react to form monomers ([AB]). In the second stage, the aggregation of monomers induces the formation of embryos, also termed as the burst nucleation stage[43]. The collision of embryos with surrounding monomers results in size increase. The embryos with size over the critical nucleation radius (r*) are stable in the reaction medium, denoted as nuclei. In the third stage, the nuclei are proceeded the subsequent diffusion-controlled growth into larger nanocrystals. These three stages correspond to the , , and in the Lamer model in Fig. 2b respectively. Assuming that when the monomer concentration is less than C^*_{min}, and the nucleation (stage) is effectively stopped. For monodisperse nanocrystals synthesis, if Ostwald ripening is not considered, the final size (R_f) of resulted nanocrystals is mainly determined by the ratio between total amount of monomers and the total number of nuclei (N_{nuclei}). And R_f can be calculate using Eq. 1.

$$R_f = \sqrt[3]{\frac{3\varphi M_{total}}{4\pi N_{nuclei}}} \quad (1)$$

where M_{total} is the total amount of monomers, φ is the proportion of atomic volume in unit cell.

Although, many previous works have derived the equation of nucleation rate (*dN/dt*) from chemical dynamics, it is still great challenge to calculate the N_{nuclei} due to the difficulty in determining the nucleation time[17, 19–21, 44,45]. In this work, we try to correlate the N_{nuclei} with *r** from the viewpoint of thermodynamics. Based on the experimental results and previous theoretical models, we developed the nuclei number-considered Lamer model based on the Maxwell-Boltzmann distribution of embryos, which enable us to estimate the maximum final size of monodispersed nanocrystals.

From the viewpoint of thermodynamics, we here proposed that the size distribution of embryos (produced in the nucleation stage) follows a Maxwell-Boltzmann statistic as Eq. 2[46].

$$\Delta N_r/N_m = Ae^{\frac{12\pi r^2 v_m \gamma - 4\pi r^3 RTln\omega}{3v_m kT}} \quad (2)$$

where ΔN_r is the number of embryos of size *r*, N_m is the total number of monomers, *A* is the pre-exponential factor, v_m is the molar volume of the crystal, *γ* is the specific surface energy, *R* is the gas constant, and *T* is the absolute temperature, *ω* is the supersaturation of reactional solution, *k* is the Boltzmann constant. Figure 2c shows the general profile of Maxwell-Boltzmann distribution of embryos sizes at a constant temperature at which the nucleation conducted. Hence, the N_{nuclei} can be estimated by the integral of the size distribution function (*r** to ∞). Based on the above discussion, the value of *r** is the key factor to determine the final size of nanocrystals using one-step injection method.

According to the classical Gibbs equation, the *r** can be derived as Eq. 3[17], and according to the modified Gibbs-Thompson equation, the *r** can also be described as Eq. 4[47], quantitatively, the r* found in Eq. 4 is 1/3 larger in size than the valve shown in Eq. 3. However, the Gibbs-based equations are not self-consistent, because the derived r* in the Gibbs methods neglect the size effect and solvent coordination effect of surface energy. In fact, the value of *γ* of nanoparticle is strongly correlated with its size, surface ligands and solvent medium[48,49]. Basically, ligands “push” on the surface of nucleus to stabilize it by moderating the surface energy[48]. The binding affinity between ligands and as-formed strongly affects the surface energy of nucleus. Whereas a more in-depth theoretical argument of *r** is in development. Qualitatively, *r** strongly relates to *γ* and the *ω* of reaction medium, which is proportional to *γ* and

inversely proportional to ω if set reaction temperature as constant. Here, we proposed a modified formula to describe γ based on previous studies[49,50], as shown in Eq. 5.

$$r^*(1) = \frac{2\gamma v_m}{RTIn\omega} \quad (3)$$

$$r^*(2) = \frac{8\gamma v_m}{3RTIn\omega} \quad (4)$$

$$\gamma(r, Ligand) = \gamma(r) - N_L \delta E_{bond} \quad (5)$$

where $\gamma(r)$ is the proportion of size dependent surface energy, it was described in different formula using different model[51], N_L is the number of ligands bonded to nanocrystalline surface atoms, δ is the surface energy correction factor, E_{bond} is the bond energy between ligand and nanocrystalline surface atom.

We further analyzed the experimental results of ZnSe nanocrystals synthesis. As shown in Fig. 1g, the final size of ZnSe nanocrystals decrease with the increasing of OA concentration. Based on the proposed model above, the strong binding affinity between OA and ZnSe nuclei induced the surface energy of ZnSe nuclei decreasing, resulting in the decrease of r^*. As a sequence, the N_{nuclei} increased with the OA concentration increasing (as shown in figure S8 and Table S1). Therefore, according to Eq. 1, the increase of the total number of ZnSe nuclei accounts for the final size of ZnSe nanocrystals decreasing. As discussed above, except for γ, ω also determined the value of r^*. We further investigated the influence of initial supersaturation (precursor concentration) on the as-formed total number of nuclei. As shown in figure S7, the final size of resulted ZnSe nanocrystals decreased with precursor concentration increasing. The increase of precursor concentration resulted in the increase of ω, thus induce the decrease of r^*. As a sequence, the decrease of ZnSe nanocrystals' size with precursors concentration increasing can be explained to the increase of N_{nuclei}. It is concluded that the nucleation process in ZnSe nanocrystals synthesis can be well described by the nuclei number-considered Lamer model based on the Maxwell-Boltzmann distribution of embryos.

In the stage , the diffusion-controlled growth is limited by the diffusion of monomers to the nuclei. For the growth of ZnSe nanocrystals, to address the existing challenges in the synthesis of large-sized ZnSe nanocrystals, we further analyzed the diffusion-controlled growth of ZnSe nanocrystals. Assuming nanocrystal grows layer-by-layer, all monomers in the diffusion sphere can diffuse to the surface of preformed ZnSe nanocrystal to satisfy the requirement of one layer's growth, as shown in figure S16. Figure 2d illustrates the calculation result of evolution of the diffusion radius (R_D) with R during one-step growth. When the diffusion spheres in the reaction system are tangent, the radius of diffusion sphere is

defined as the critical diffusion radius. R_D increases dramatically when it reaches the critical point, indicating the further growth of nanocrystal becomes extremely difficult. The size evolution of ZnSe nanocrystals with time prolonging can be predicted by considering the monomers concentration in solution (C_L) over time (shown in SI, diffusion-controlled growth model section), which in line with our experimental results and the above discussions. Therefore, we draw a conclusion that the final size of ZnSe nanocrystals obtained from hot-injection synthesis has a critical value. The value of the final size can be varied by tunning the reactivity of Zn and Se precursors or their concentration. To our knowledge, there is no existed reaction system to obtain large-sized ZnSe nanocrystals with expected size (over 10 nm) for pure blue emitting applications (SI, Extended Data Table S2).

Reactivity-Controlled Epitaxial Growth (RCEG) of large-sized ZnSe nanocrystals.

Epitaxial growth is typical methodology to grow large-sized core shell nanocrystals, which is realized via continuous injection of precursors into small-sized seeds[52–54]. Nevertheless, secondary nucleation events are very easy to occur during the continuous injection of precursors, which leads to size-broadening. The epitaxial growth conditions need to be carefully chosen, especially the replenishment rate of the precursors[55]. In our work, by optimizing the reactivity of continuous injected precursors, we developed a versatile strategy of reactivity-controlled epitaxial growth for fabricating large-sized spherical ZnSe nanocrystals with pure-blue emission by sequential injection of high-reactivity and low-reactivity Zn (Se) precursors. The secondary nucleation during epitaxial growth was suppressed by adding low reactivity precursors. In a typical synthesis, high reactivity Zn and Se precursors are employed for fabricating ZnSe seeds, while low reactivity Zn and Se precursors are added for further epitaxial growth into large-sized ZnSe nanocrystals.

Figure 3a schematically shows the procedure of RCEG strategy. By injecting Se-DPP into the precursor solution of OA-$Zn(OAc)_2$-OLA (OA : OLA = 0.2 : 1) at 280°C then followed the growth at 300°C, ZnSe seeds with small size of 4.0 nm can be fabricated. After that, a mixed precursor solution of Se-ODE and OA-$Zn(OAc)_2$-OLA (OA : OLA = 1 : 1) was continuously added into the reaction medium to realize the epitaxial growth of ZnSe nanocrystals with diameter over 10 nm. Figure 3b-3c show the evolution of the UV-vis absorption and PL spectra with the RCEG synthesis prolonging, Excitingly, the PL peaks of these ZnSe nanocrystals shifted from 425 nm to 470 nm during the RCEG process, and a sample with FWHM of 25 nm at 460 nm was obtained. As shown in the TEM images (Fig. 3d-3f), the obtained large-sized ZnSe nanocrystals are monodispersed with narrow size distribution. The average sizes of these samples are 8.3 nm, 10.3 nm, 13.4 nm, 17.6 nm, 27.1 nm, and 35.2 nm, respectively. The XRD characterizations shown in figure S10 indicate that these samples are of zinc blende structure.

Fabricating of large-sized ZnSe/ZnS core-shell nanocrystals.

To enhance the PL efficiency and photostability of large-sized ZnSe nanocrystals, ZnS (bandgap, 3.7eV) was chosen as shell coating to passivate the surface defects of ZnSe nanocrystals. In our work, we used ZnSe nanocrystals with average diameter of ~9 nm, PL peak of 455 nm, FWHM of 22 nm, and PLQY of

23% for shell coating. The ZnS shell coating was performed by successively injecting S-TOP (to form the first layer of ZnS shell, marked as ZnS1) and pre-prepared Zn-S precursors (to form the second layer of ZnS shell, marked as ZnS2). Figure 4a shows the evolution of the absorption and PL spectra after the ZnS shell growth on the ZnSe cores. The absorbance at 365 nm remained the same, and the absorbance at 300 nm increased after the epitaxial growth of ZnS on the surface of ZnSe cores, indicating that ZnS was successfully coated on ZnSe cores. Figure 4b shows the evolution of PLQY, PL peak, and FWHM during the ZnS shell growth. The PLQY reach to 60% as the shell thickness increased to ~4 MLs and then started to decrease indicating the occurrence of interfacial strain-related defects[12]. Upon growth of the ZnS shell, three major diffraction peaks shifted to higher angles due to the smaller ZnS lattice constant compared with ZnSe (Fig. 4c). Figure 4d-4f provide the TEM, HRTEM and corresponding fast Fourier Transform (FFT) images of ZnSe, ZnSe/ZnS1 and ZnSe/ZnS2, respectively. Both of lattice structure and FFT correspond to the zinc-blende structure. Such large-sized ZnSe/ZnS core-shell nanocrystals show pure blue emission (~455 nm) and narrow ensemble PL width (~22 nm), which are ideal emitter for display applications.

RCEG of large-sized CdSe and PbSe nanocrystals.

To verify the generality of the RCEG strategy for large-sized nanocrystals synthesis, we further fabricated large-sized CdSe and PbSe nanocrystals. Firstly, monodispersed small-sized CdSe and PbSe seeds (< 5 nm, the TEM images were shown in figure S14a and figure S15a) were obtained through hot-injection method. Then, epitaxial growth of CdSe and PbSe seeds was achieved by continuous injection of moderate-reactivity cations and anions precursors. Note that during the nucleation and growth process, after employing our precise reactivity regulating strategy of precursors, secondary nucleation can be effectively suppressed. Figure 5 and figure S14-S15 show the TEM images of CdSe and PbSe nanocrystals that fabricated with different amount of precursors injection. The largest size of obtained CdSe and PbSe nanocrystals approach to 76.3 nm and 86.6 nm, respectively. Their size distribution is exceedingly narrow, about 10% in coefficient of variation (= standard deviation/mean size).

Conclusion

In summary, we investigated the reactivity of Zn and Se precursors to illustrate the key factors in determining the final size of ZnSe nanocrystals via hot-injection method. It was found that the final size can be significantly varied by using different precursors and ligands. We further illustrated that the final size of nanocrystal synthesis has a critical value that is mainly determined by the total number of nuclei. A nuclei number-considered Lamer model based on the Maxwell-Boltzmann distribution of embryos was developed to describe the influence of precursors and ligands on the critical nucleation radius, which provide insights into the correlations between the critical nucleation radius and total number of nuclei. Based on this understanding, we designed a general RCEG strategy to synthesize large-sized ZnSe, CdSe and PbSe nanocrystals with average size over 35 nm, 76 nm, 86 nm, respectively. The resulted large-sized ZnSe nanocrystals show strong PL emission with peak up to 470 nm. We further fabricated efficient and stable large-sized ZnSe/ZnS core-shell QDs with quantum yields up to 60%. We believe that the

hybridization of quantum confined and classical effects in these large-sized semiconductor nanocrystals provides new opportunities for basic research and applications.

Methods

Chemicals and reagents. All reagents were used as received without further experimental purification.

1-octadecene (ODE, 90%), oleic acid (OA, 90%), oleylamine (OLA, 90%), octanethiol (OT, 98%), Diphenylphosphine (DPP, 97%), Trioctylphosphine (TOP, 90%), zinc acetate ($Zn(OAc)_2$, 99.99%) and selenium (Se, 99.99%, powder), sulfur (S, 99.99%, powder), cadmium oxide (CdO, 99.99%), lead oxide (PbO, 99.99%) were purchased from Aldrich.

Hot-injection synthesis of original ZnSe seeds

For synthesis of original ZnSe seeds, the hot-injection method was used. First, to prepare [0.4M] Se-DPP stock solution, 0.48 mmol of Se was dissolved in 1.2 mL of DPP in N_2 filled glove box. The mixture was heated and became transparent faint yellow solution and kept in glove box for further use. Then, 0.4 mmol of zinc acetate, 0.2 mL of OA, 1 mL of OLA and 10 mL of liquid paraffin were placed in a three-neck flask by stirring (900 r/min) and heated to 120°C under vacuum and kept at this temperature for 40 min. After the atmosphere was changed to N_2, the mixed solution was heated to 280°C, at which temperature 0.5 mL of Se-DPP was quickly injected. Subsequently, the temperature was increased to 300°C and reacted at this temperature for 30 min.

Epitaxial Growth of large-sized ZnSe nanocrystals

To obtain large-sized ZnSe nanocrystals, the RCEG method was used, Zn-Se precursor was continuously injected into the original ZnSe seeds solution at a rate of 3.6 mL per hour at 300°C. The Zn-Se precursor was prepared by mixing low-reactivity Zn and Se stock solution. Zn stock solution was prepared by mixing 8 mmol of zinc acetate, 3 mL of OA, 3 mL of OLA and 14 mL of ODE solvent in a three-neck flask by stirring, and the mixture was heated to 120°C under vacuum and kept at that temperature for 40 min. After the atmosphere was changed to N_2, the mixed solution was heated to 160°C until it became transparent faint yellow solution, then cooled down to 100°C for further use. Se stock solution was prepared by mixing 4 mmol of Se powder and 10 mL of ODE solvent, and the mixed solution was firstly heated to 220°C for 30 min, then heated at 240°C until it became transparent brown solution, then cooled down to 100°C for further use.

Synthesis of ZnSe/ZnS core shell nanocrystals

First, to prepared Zn-S precursor. 8 mmol of Zn acetate, 8 mmol (1.6 mL) of OT, 3 mL of OLA and 35.4 mL of ODE were mixed in a three-neck flask with vigorous stirring. And the mixture was heated to 120°C under vacuum and kept at that temperature for 40 min to obtain colorless transparent solution. Then cooled to 80°C for following use. To facilitate the growth of the first ZnS shell, 0.2 M TOP-S were added

into the ZnSe core solution and further reacted for 1.5 h at 300°C to form the first layer of ZnS shell, marked as ZnSe/ZnS1. After that, the solution was cooled to 280°C for the second shell coating. The above Zn-S precursor was continually injected (6 mL/h) into the reaction medium to form the second layer of ZnS shell, marked as ZnSe/ZnS2. Here, we balanced the precursor concentrations to control the reaction rates for the growth of the core and each shell, and maintained the metal precursor excess during the reaction.

Purification of ZnSe and ZnSe/ZnS nanocrystals. The crude ZnSe and ZnSe/ZnS nanocrystals solution was dissolved in hexane with a volume ratio of 1:1, which was precipitated by adding ethanol with volume ratio of 1:2 and then centrifugation. The resulted ZnSe and ZnSe/ZnS nanocrystals products were purified by this method for three times and redispersed in hexane for further use.

RCEG of large-sized CdSe nanocrystals.

For synthesis of CdSe seeds, 0.4 mmol of CdO, 0.5 mL of OA, 1 mL of OLA and 10 mL of ODE were placed in a three-neck flask by stirring (900 r/min) and heated to 120°C under vacuum and kept at this temperature for 40 min. After the atmosphere was changed to N_2, the mixed solution was heated to 280°C. Subsequently, 0.5 mL of 0.4 M Se-TOP was quickly injected into the mixed solution and further reacted for 30 min to produce CdSe seeds. For synthesis of large-sized CdSe nanocrystals, the RCEG method was used, Cd-Se precursor was continuously injected into the original CdSe seeds solution at a rate of 3.6 mL/h at 260°C.

RCEG of large-sized PbSe nanocrystals.

For synthesis of PbSe seeds, 0.4 mmol of PbO, 1 mL of OA and 10 mL of ODE were placed in a three-neck flask by stirring (900 r/min) and heated to 120°C under vacuum and kept at that temperature for 40 min. After the atmosphere was changed to N_2, the mixed solution was heated to 220°C. Subsequently, 0.5 mL of 0.4 M Se-TOP was quickly injected into the mixed solution, and the temperature was kept at 220°C, and further reacted for 30min. For synthesis of large-sized PbSe nanocrystals, the RCEG method was used, Pb-Se precursor was continuously injected into the original PbSe seeds solution at a rate of 3.6 mL/h at 200°C.

The Characterization of ZnSe nanocrystals sizes.

Based on our PL spectra and TEM characterization results (shown in SI, figure S11) of ZnSe nanocrystals, we plot the experimental results of PL peaks versus diameters of ZnSe nanocrystals and their fitting result (figure S9) expressed in a power law relation as following. And according to these two formulas, we can calculate the diameter of ZnSe nanocrystals from their PL peak.

$$W_{peak} = 476.02 \times \frac{D_{Crys}^{1.42}}{1.08^{1.42} + D_{Crys}^{1.42}} \qquad R^2 = 0.999 \qquad (1)$$

$$D_{Crys} = 2.76 + 8.59 \times 10^{-4} \times e^{\frac{W_{peak}-421.86}{5.21}} + 1.78 \times e^{\frac{W_{peak}-421.86}{26.88}} \qquad R^2 = 0.999 \qquad (2)$$

Absorption and PL spectroscopy. Steady-state ultraviolet–visible (UV-vis) absorption spectra were measured by using a UV-6100 UV-vis spectrophotometer (Shanghai Mapada Instruments Co., Ltd.). PL spectra were measured by using a F-380 fluorescence spectrometer (Tianjin Gangdong Science and Technology Development Co., Ltd.).

PL quantum yield.

The PL QY of the samples was measured under the excitation at 365 nm in comparison with 9,10-diphenylanthracene (DPA) in cyclohexane as the reference. DPA with a high absolute PLQY of 95%, usually used as reference for PLQY testing.

$$QY_S = QY_R \times \frac{I_S}{I_R} \times \frac{A_R}{A_S} \times \frac{n_S^2}{n_R^2}$$

Where QY_S and QY_R is the QY of sample and reference, respectively. I_S, I_R are the integral area of the spectrum of sample and reference, respectively. A_S, A_R are the absorbance of sample and reference, respectively. n_S, n_R are the refractive index of sample and reference solvent, respectively.

TEM images. All TEM images were acquired on a FEI Talos F200S field-emission transmission electron microscope (FEI Co., USA) operated at 200 kV.

XRD patterns. A BRUKER D8 advance X-ray diffractometer equipped with a Cu Kα radiation source was used to record the X-ray diffraction (XRD) patterns.

Declarations

Competing interests

The authors declare no competing interests.

References

1. García de Arquer, F. P.; Talapin, D. V.; Klimov, V. I.; Arakawa, Y.; Bayer, M.; Sargent, E. H., Semiconductor quantum dots: Technological progress and future challenges. Science 2021, *373* (6555), eaaz8541.

2. Efros, A. L.; Brus, L. E., Nanocrystal Quantum Dots: From Discovery to Modern Development. ACS nano **2021**, *15* (4), 6192–6210.
3. Shirasaki, Y.; Supran, G. J.; Bawendi, M. G.; Bulović, V., Emergence of colloidal quantum-dot light-emitting technologies. Nature photonics 2013, *7* (1), 13–23.
4. Won, Y.-H.; Cho, O.; Kim, T.; Chung, D.-Y.; Kim, T.; Chung, H.; Jang, H.; Lee, J.; Kim, D.; Jang, E., Highly efficient and stable InP/ZnSe/ZnS quantum dot light-emitting diodes. Nature 2019, *575* (7784), 634–638.
5. Shu, Y.; Lin, X.; Qin, H.; Hu, Z.; Jin, Y.; Peng, X., Quantum dots for display applications. Angewandte Chemie International Edition 2020, *59* (50), 22312–22323.
6. Jang, E.; Kim, Y.; Won, Y.-H.; Jang, H.; Choi, S.-M., Environmentally friendly InP-based quantum dots for efficient wide color gamut displays. ACS Energy Letters 2020, *5* (4), 1316–1327.
7. Kim, B. H.; Onses, M. S.; Lim, J. B.; Nam, S.; Oh, N.; Kim, H.; Yu, K. J.; Lee, J. W.; Kim, J.-H.; Kang, S.-K., High-resolution patterns of quantum dots formed by electrohydrodynamic jet printing for light-emitting diodes. Nano letters **2015**, *15* (2), 969–973.
8. Zhang, M.; Hu, B.; Meng, L.; Bian, R.; Wang, S.; Wang, Y.; Liu, H.; Jiang, L., Ultrasmooth quantum dot micropatterns by a facile controllable liquid-transfer approach: low-cost fabrication of high-performance QLED. Journal of the American Chemical Society 2018, *140* (28), 8690–8695.
9. Kim, T.; Kim, K.-H.; Kim, S.; Choi, S.-M.; Jang, H.; Seo, H.-K.; Lee, H.; Chung, D.-Y.; Jang, E., Efficient and stable blue quantum dot light-emitting diode. Nature 2020, *586* (7829), 385–389.
10. Hines, M. A.; Guyot-Sionnest, P., Bright UV-blue luminescent colloidal ZnSe nanocrystals. The Journal of Physical Chemistry B **1998**, *102* (19), 3655–3657.
11. Li, L. S.; Pradhan, N.; Wang, Y.; Peng, X., High quality ZnSe and ZnS nanocrystals formed by activating zinc carboxylate precursors. Nano letters 2004, *4* (11), 2261–2264.
12. Ji, B.; Koley, S.; Slobodkin, I.; Remennik, S.; Banin, U., ZnSe/ZnS core/shell quantum dots with superior optical properties through thermodynamic shell growth. Nano letters **2020**, *20* (4), 2387–2395.
13. Gao, M.; Yang, H.; Shen, H.; Zeng, Z.; Fan, F.; Tang, B.; Min, J.; Zhang, Y.; Hua, Q.; Li, L. S., Bulk-like ZnSe Quantum Dots Enabling Efficient Ultranarrow Blue Light-Emitting Diodes. Nano Letters 2021, *21* (17), 7252–7260.
14. Murray, C.; Norris, D. J.; Bawendi, M. G., Synthesis and characterization of nearly monodisperse CdE (E = sulfur, selenium, tellurium) semiconductor nanocrystallites. Journal of the American Chemical Society **1993**, *115* (19), 8706–8715.
15. Peng, X.; Wickham, J.; Alivisatos, A., Kinetics of II-VI and III-V colloidal semiconductor nanocrystal growth:“focusing” of size distributions. Journal of the American Chemical Society 1998, *120* (21), 5343–5344.
16. Peng, Z. A.; Peng, X., Nearly monodisperse and shape-controlled CdSe nanocrystals via alternative routes: nucleation and growth. Journal of the American Chemical Society 2002, *124* (13), 3343–3353.

17. Park, J.; Joo, J.; Kwon, S. G.; Jang, Y.; Hyeon, T., Synthesis of monodisperse spherical nanocrystals. Angewandte Chemie International Edition 2007, *46* (25), 4630–4660.
18. Owen, J. S.; Chan, E. M.; Liu, H.; Alivisatos, A. P., Precursor conversion kinetics and the nucleation of cadmium selenide nanocrystals. Journal of the American Chemical Society 2010, *132* (51), 18206–18213.
19. Lee, J.; Yang, J.; Kwon, S. G.; Hyeon, T., Nonclassical nucleation and growth of inorganic nanoparticles. Nature Reviews Materials **2016**, *1* (8), 1–16.
20. Liu, M.; Wang, K.; Wang, L.; Han, S.; Fan, H.; Rowell, N.; Ripmeester, J. A.; Renoud, R.; Bian, F.; Zeng, J., Probing intermediates of the induction period prior to nucleation and growth of semiconductor quantum dots. Nature communications **2017**, *8* (1), 1–12.
21. Leffler, V.; Ehlert, S.; Förster, B.; Dulle, M.; Förster, S., Nanoparticle Heat-Up Synthesis: In Situ X-ray Diffraction and Extension from Classical to Nonclassical Nucleation and Growth Theory. ACS nano 2021, *15* (1), 840–856.
22. Qu, L.; Peng, Z. A.; Peng, X., Alternative routes toward high quality CdSe nanocrystals. Nano letters 2001, *1* (6), 333–337.
23. Talapin, D. V.; Rogach, A. L.; Kornowski, A.; Haase, M.; Weller, H., Highly luminescent monodisperse CdSe and CdSe/ZnS nanocrystals synthesized in a hexadecylamine – trioctylphosphine oxide – trioctylphospine mixture. Nano letters 2001, *1* (4), 207–211.
24. Chen, Y.; Vela, J.; Htoon, H.; Casson, J. L.; Werder, D. J.; Bussian, D. A.; Klimov, V. I.; Hollingsworth, J. A., "Giant" multishell CdSe nanocrystal quantum dots with suppressed blinking. Journal of the American Chemical Society 2008, *130* (15), 5026–5027.
25. Chen, O.; Zhao, J.; Chauhan, V. P.; Cui, J.; Wong, C.; Harris, D. K.; Wei, H.; Han, H.-S.; Fukumura, D.; Jain, R. K., Compact high-quality CdSe–CdS core–shell nanocrystals with narrow emission linewidths and suppressed blinking. Nature materials **2013**, *12* (5), 445–451.
26. Manna, L.; Scher, E. C.; Alivisatos, A. P., Synthesis of soluble and processable rod-, arrow-, teardrop-, and tetrapod-shaped CdSe nanocrystals. Journal of the American Chemical Society 2000, *122* (51), 12700–12706.
27. Liu, L.; Zhuang, Z.; Xie, T.; Wang, Y.-G.; Li, J.; Peng, Q.; Li, Y., Shape control of CdSe nanocrystals with zinc blende structure. Journal of the American Chemical Society 2009, *131* (45), 16423–16429.
28. Peng, X.; Manna, L.; Yang, W.; Wickham, J.; Scher, E.; Kadavanich, A.; Alivisatos, A. P., Shape control of CdSe nanocrystals. Nature 2000, *404* (6773), 59–61.
29. Ithurria, S.; Dubertret, B., Quasi 2D colloidal CdSe platelets with thicknesses controlled at the atomic level. Journal of the American Chemical Society 2008, *130* (49), 16504–16505.
30. Zhong, H.; Scholes, G. D., Shape tuning of type II CdTe-CdSe colloidal nanocrystal heterostructures through seeded growth. Journal of the American Chemical Society **2009**, *131* (26), 9170–9171.
31. Jia, G.; Banin, U., A general strategy for synthesizing colloidal semiconductor zinc chalcogenide quantum rods. Journal of the American Chemical Society **2014**, *136* (31), 11121–11127.

32. Ning, J.; Liu, J.; Levi-Kalisman, Y.; Frenkel, A. I.; Banin, U., Controlling anisotropic growth of colloidal ZnSe nanostructures. Journal of the American Chemical Society **2018**, *140* (44), 14627–14637.
33. Ji, B.; Panfil, Y. E.; Waiskopf, N.; Remennik, S.; Popov, I.; Banin, U., Strain-controlled shell morphology on quantum rods. Nature communications 2019, *10* (1), 1–9.
34. Acharya, S.; Sarma, D.; Jana, N. R.; Pradhan, N., An alternate route to high-quality ZnSe and Mn-doped ZnSe nanocrystals. The Journal of Physical Chemistry Letters **2010**, *1* (2), 485–488.
35. Jang, E.-P.; Han, C.-Y.; Lim, S.-W.; Jo, J.-H.; Jo, D.-Y.; Lee, S.-H.; Yoon, S.-Y.; Yang, H., Synthesis of alloyed ZnSeTe quantum dots as bright, color-pure blue emitters. ACS applied materials & interfaces 2019, *11* (49), 46062–46069.
36. Wei, S.-H.; Zhang, S.; Zunger, A., First-principles calculation of band offsets, optical bowings, and defects in CdS, CdSe, CdTe, and their alloys. Journal of applied Physics 2000, *87* (3), 1304–1311.
37. Guo, Y.; Alvarado, S. R.; Barclay, J. D.; Vela, J., Shape-programmed nanofabrication: Understanding the reactivity of dichalcogenide precursors. ACS nano 2013, *7* (4), 3616–3626.
38. Toufanian, R.; Zhong, X.; Kays, J. C.; Saeboe, A. M.; Dennis, A. M., Correlating ZnSe Quantum Dot Absorption with Particle Size and Concentration. Chemistry of Materials **2021**, *33* (18), 7527–7536.
39. LaMer, V. K.; Dinegar, R. H., Theory, production and mechanism of formation of monodispersed hydrosols. Journal of the american chemical society **1950**, *72* (11), 4847–4854.
40. Kashchiev, D., *Nucleation*. Elsevier: 2000.
41. Rempel, J. Y.; Bawendi, M. G.; Jensen, K. F., Insights into the kinetics of semiconductor nanocrystal nucleation and growth. Journal of the American Chemical Society **2009**, *131* (12), 4479–4489.
42. Thanh, N. T.; Maclean, N.; Mahiddine, S., Mechanisms of nucleation and growth of nanoparticles in solution. Chemical reviews **2014**, *114* (15), 7610–7630.
43. Robb, D. T.; Privman, V., Model of nanocrystal formation in solution by burst nucleation and diffusional growth. Langmuir 2008, *24* (1), 26–35.
44. Abe, S.; Capek, R. K.; De Geyter, B.; Hens, Z., Tuning the postfocused size of colloidal nanocrystals by the reaction rate: from theory to application. ACS nano 2012, *6* (1), 42–53.
45. Sosso, G. C.; Chen, J.; Cox, S. J.; Fitzner, M.; Pedevilla, P.; Zen, A.; Michaelides, A., Crystal nucleation in liquids: Open questions and future challenges in molecular dynamics simulations. Chemical reviews 2016, *116* (12), 7078–7116.
46. Leite, E. R.; Ribeiro, C., *Crystallization and growth of colloidal nanocrystals*. Springer Science & Business Media: 2011.
47. Xie, R.; Li, Z.; Peng, X., Nucleation kinetics vs chemical kinetics in the initial formation of semiconductor nanocrystals. Journal of the American Chemical Society 2009, *131* (42), 15457–15466.
48. Scholes, G. D., Controlling the optical properties of inorganic nanoparticles. Advanced Functional Materials 2008, *18* (8), 1157–1172.
49. Sugimoto, T., *Monodispersed particles*. Elsevier: 2019.

50. Fokin, V. M.; Zanotto, E. D., Crystal nucleation in silicate glasses: the temperature and size dependence of crystal/liquid surface energy. Journal of non-crystalline solids 2000, *265* (1–2), 105–112.
51. Schmelzer, J.; Mahnke, R., General formulae for the curvature dependence of droplets and bubbles. Journal of the Chemical Society, Faraday Transactions 1: Physical Chemistry in Condensed Phases 1986, *82* (5), 1413–1420.
52. Cozzoli, P. D.; Pellegrino, T.; Manna, L., Synthesis, properties and perspectives of hybrid nanocrystal structures. Chemical Society Reviews 2006, *35* (11), 1195–1208.
53. Carbone, L.; Nobile, C.; De Giorgi, M.; Sala, F. D.; Morello, G.; Pompa, P.; Hytch, M.; Snoeck, E.; Fiore, A.; Franchini, I. R., Synthesis and micrometer-scale assembly of colloidal CdSe/CdS nanorods prepared by a seeded growth approach. Nano letters 2007, *7* (10), 2942–2950.
54. Reiss, P.; Protiere, M.; Li, L., Core/shell semiconductor nanocrystals. *small* **2009**, *5* (2), 154–168.
55. Franke, D.; Harris, D. K.; Chen, O.; Bruns, O. T.; Carr, J. A.; Wilson, M. W.; Bawendi, M. G., Continuous injection synthesis of indium arsenide quantum dots emissive in the short-wavelength infrared. Nature communications 2016, *7* (1), 1–9.

Figures

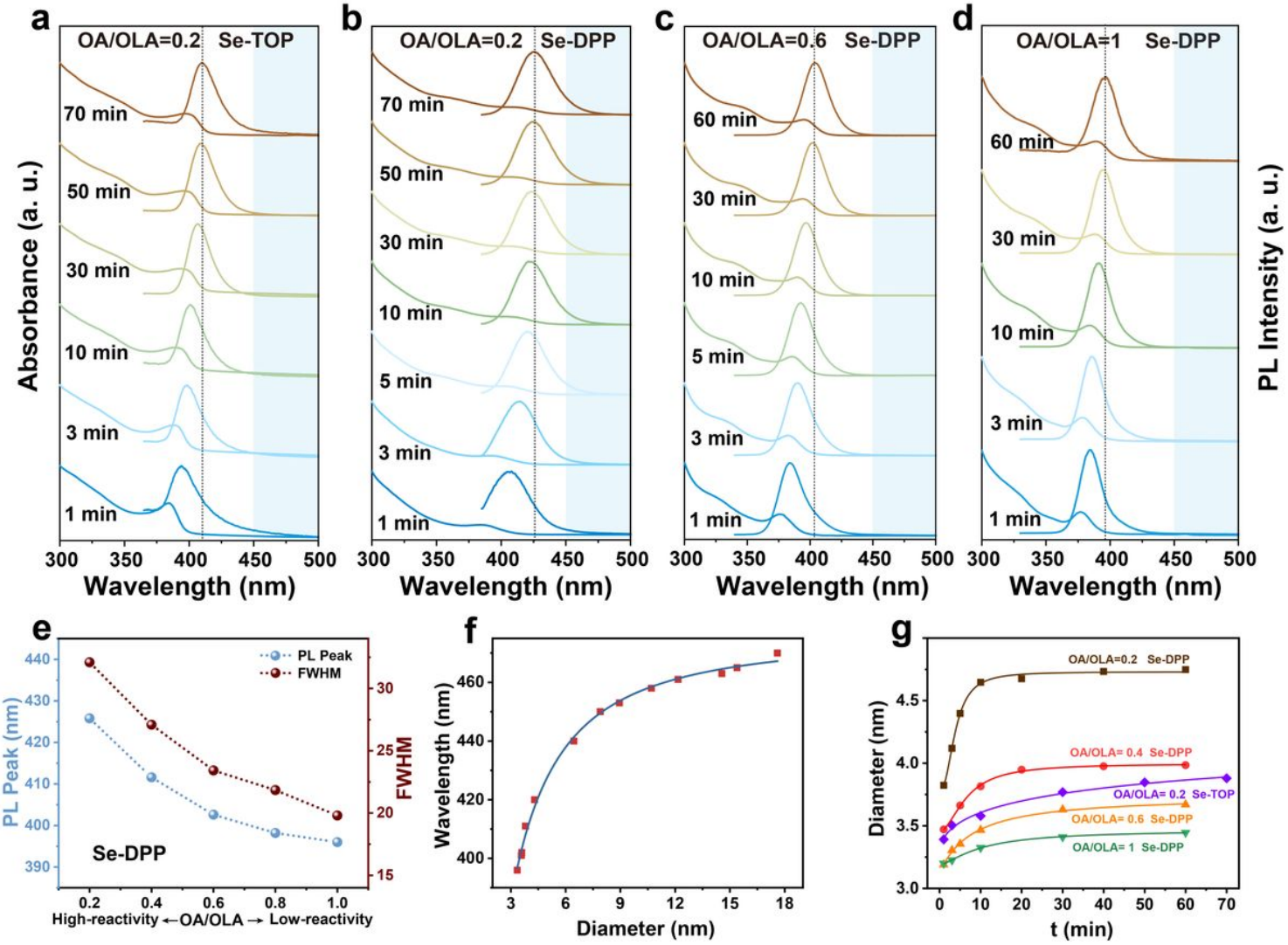

Figure 1

The synthesis of ZnSe nanocrystals through hot-injection method. Evolution of the UV-vis absorption and PL spectra of ZnSe nanocrystals, using **a,** OA-[$Zn(OAc)_2$]-OLA (OA/OLA=0.2) and Se-TOP, **b,** OA-[$Zn(OAc)_2$]-OLA (OA/OLA=0.2) and Se-DPP, **c,** OA-[$Zn(OAc)_2$]-OLA (OA/OLA=0.6) and Se-DPP, **d,** OA-[$Zn(OAc)_2$]-OLA (OA/OLA=1) and Se-DPP as precursors during a prolonged reaction time. All experiments were performed at 300°C. **e,** PL peak and FWHM of emission spectra under different OA/OLA value. **f,** Experimental results of PL peak versus diameter of ZnSe nanocrystals and their fitting result expressed in a power law relation of $W_{peak} = 476.02*D^{1.42}/(1.08^{1.42}+D^{1.42})$. **g,** Evolution of the diameter of ZnSe nanocrystals with time synthesized by varying reactivity Zn and Se precursors.

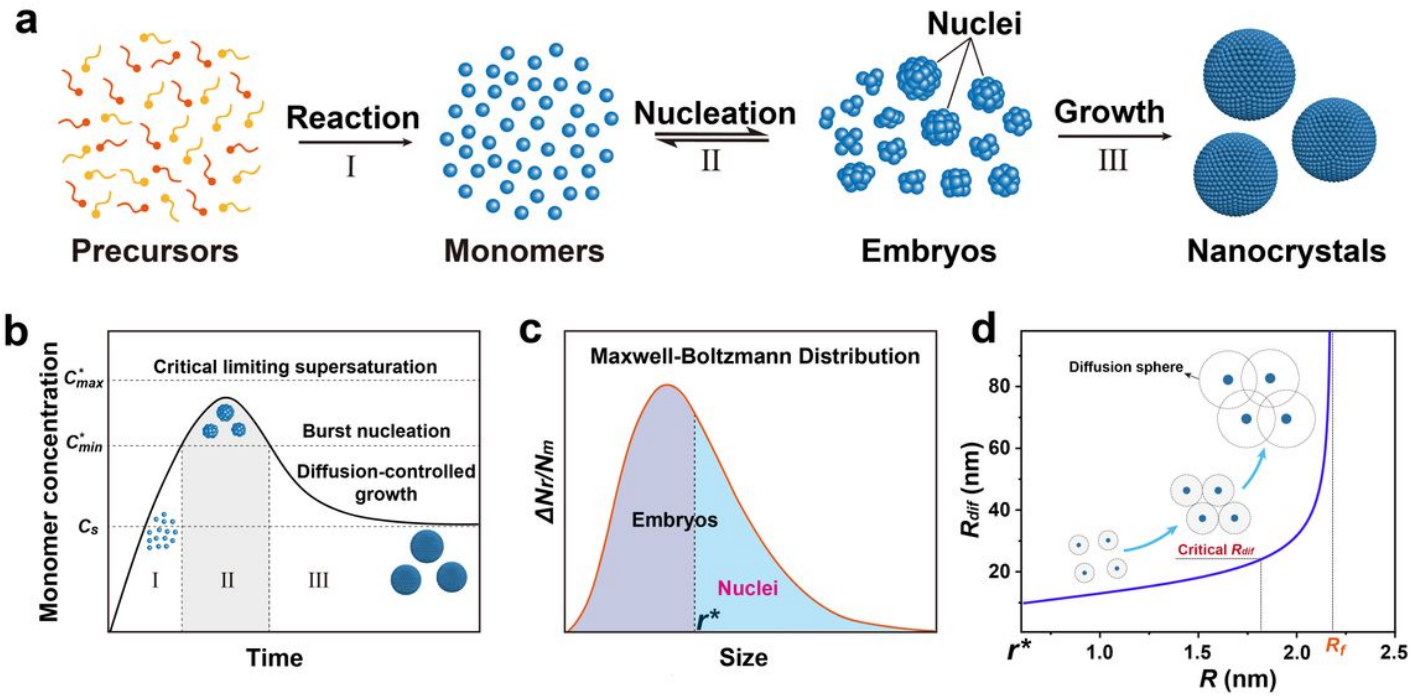

Figure 2

Nucleation and growth model of nanocrystals. a, Schematic diagram of the formation process of monodisperse nanocrystals. **b,** The classical LaMer nucleation model, which contains three stages that corresponding to the process of the formation of nanocrystals. **c,** The size distribution of crystal embryos obeys a Maxwell-Boltzmann distribution. **d,** The evolution of diffusion radius (R_{dif}) with the radius of nanocrystals (R).

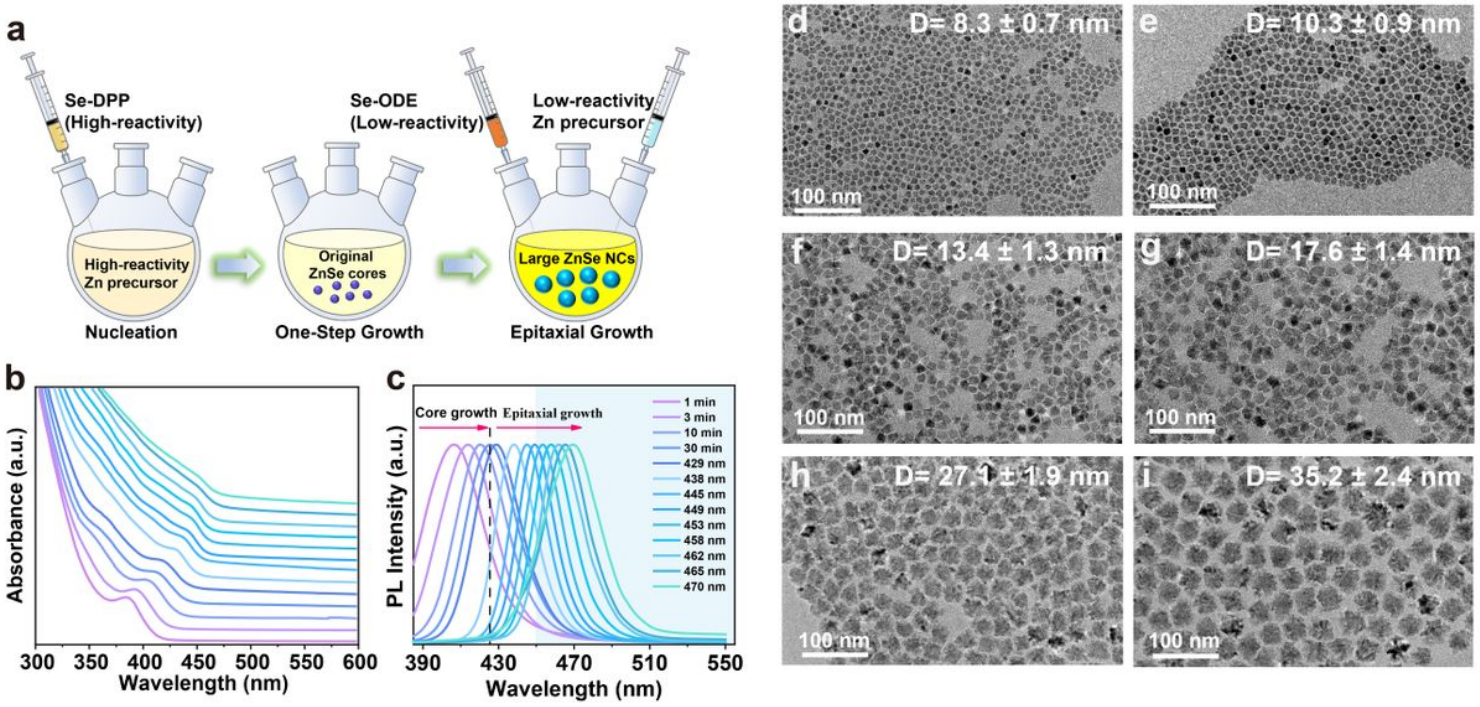

Figure 3

Epitaxial Growth of large-sized ZnSe nanocrystals. a, Schematic representation of the reactivity-controlled epitaxial growth of ZnSe nanocrystals, which features the reactivity of precursors used during the nucleation and diffusion growth stage. First, high-reactivity Zn and Se precursors were mixed to drive the formation of small-sized ZnSe seeds, and then, low-reactivity Zn and Se precursors were continually injected into the reaction system with ZnSe seeds to conduct the epitaxial growth ZnSe nanocrystals. **b,** The UV-vis absorption spectra of ZnSe nanocrystals during the growth with different first exciton absorption peak and absorption edge. **c,** The evolution of PL emission spectra of ZnSe nanocrystals during the growth process. **d,e,f,g,h,l,** The TEM images of the final ZnSe nanocrystals with different diameter synthesized by injected different amounts of Zn and Se precursors.

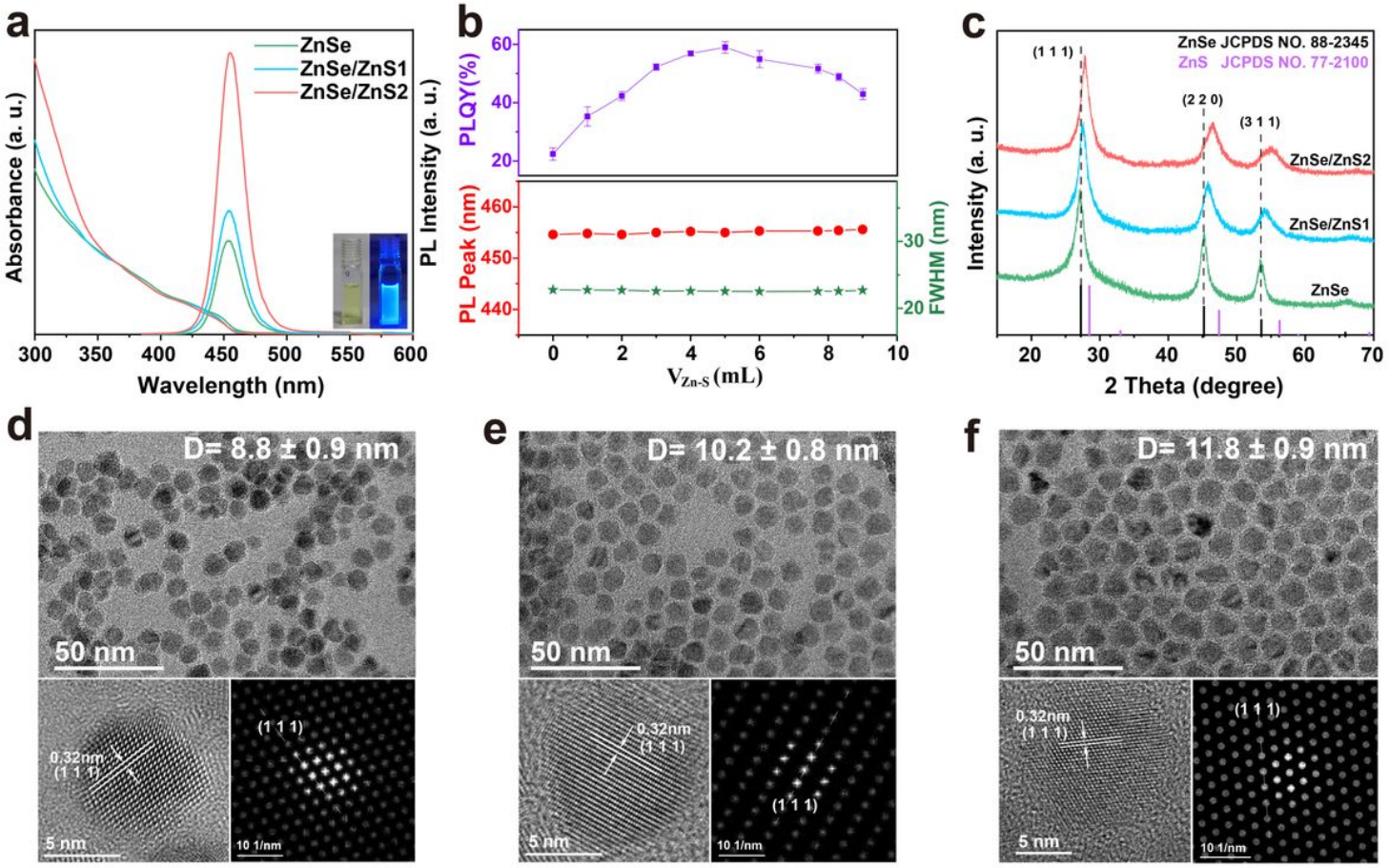

Figure 4

Optical, morphology and structural characterization of large-sized ZnSe/ZnS core-shell nanocrystals. a, The UV-vis absorption spectra, and photoluminescence spectra of ZnSe cores, ZnSe/ZnS1, ZnSe/ZnS2 nanocrystals. Inset: optical images of ZnSe/ZnS2 nanocrystals dispersed in hexane with and without illumination with a 365 nm UV lamp. **b,** Dependence of PLQY, PL peak and FWHM of ZnSe/ZnS nanocrystals the volume of shell precursor solution added. Error bars originate from repeating each QY measurement three times. **c**, XRD patterns of ZnSe cores, ZnSe/ZnS1, and ZnSe/ZnS2 nanocrystals.

TEM, HRTEM images of **d**, ZnSe core, **e**, ZnSe/ZnS1, **f**, ZnSe/ZnS2, and the corresponding Fast Fourier transform (FFT) of the whole area of a nanocrystals, which corresponds to the [111] zone axis of the cubic phase of ZnSe or ZnS.

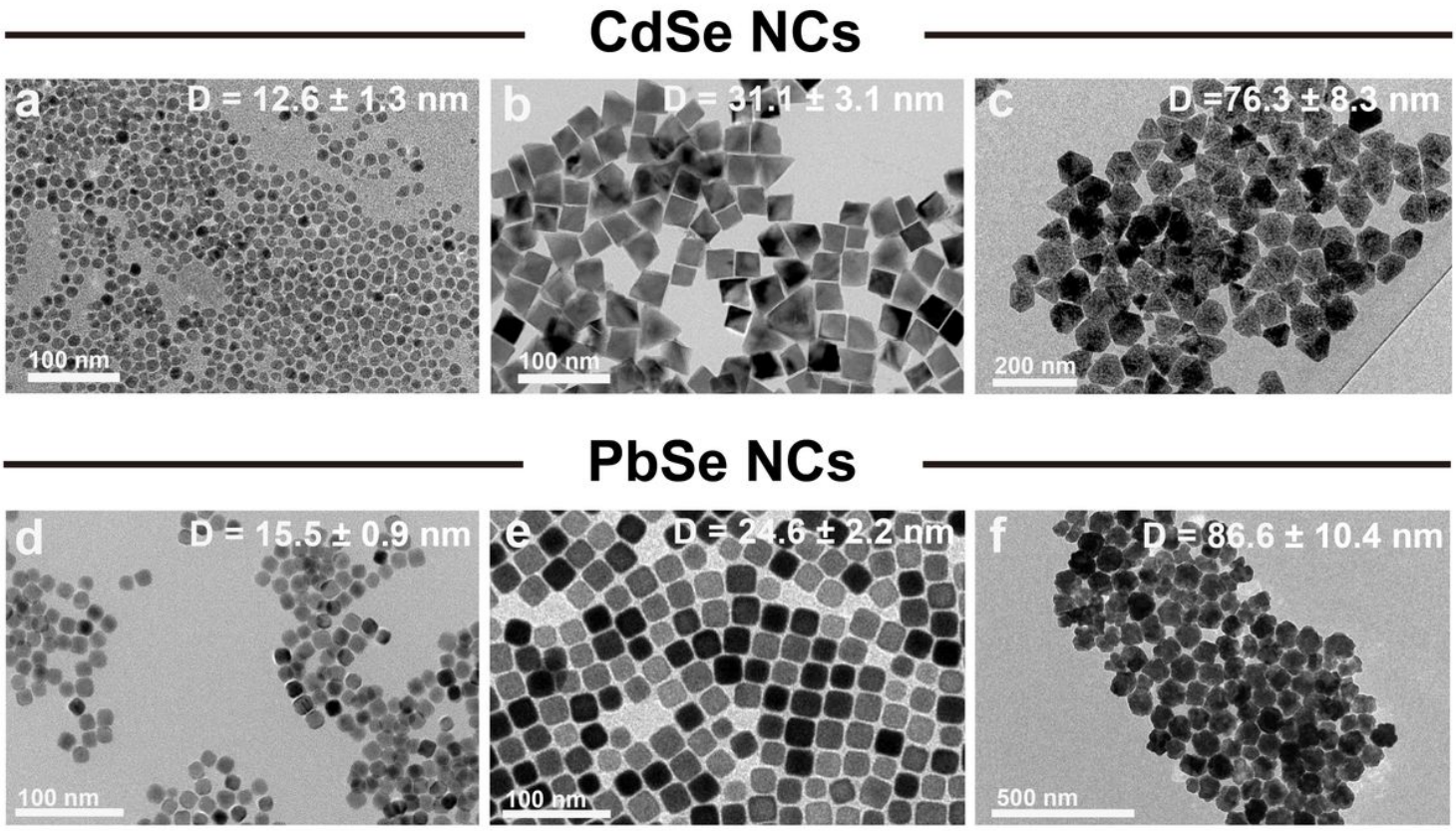

Figure 5

TEM images of large-sized CdSe and PbSe nanocrystals. CdSe nanocrystals with average sizes of **a**, 12.6 nm, **b**, 31.1 nm, **c**, 76.3 nm. PbSe nanocrystals with average size of **d**, 15.5 nm, **e**, 24.6 nm, **f**, 86.6 nm.

Supplementary Files

This is a list of supplementary files associated with this preprint. Click to download.

- AnonymitySupportingInformationCopy.docx